Monthly Notices of the ROYAL ASTRONOMICAL SOCIETY

MNRAS **519,** 4040–4046 (2023)
Advance Access publication 2022 December 22

https://doi.org/10.1093/mnras/stac3739

New Ritz wavelengths and transition probabilities for parity-forbidden, singly ionized nickel [Ni II] lines of astrophysical interest

Christian P. Clear,[1★] Peter Uylings,[2] Ton Raassen,[2,3] Gillian Nave[4] and Juliet C. Pickering[1]

[1] *Physics Department, Imperial College London, London SW7 2AZ, UK*
[2] *Anton Pannekoek Institute for Astronomy, University of Amsterdam, Science Park 904, NL-1098 XH Amsterdam, the Netherlands*
[3] *SRON Netherlands Institute for Space Research, Sorbonnelaan 2, NL-3584 CA Utrecht, the Netherlands*
[4] *National Institute of Standards and Technology, Gaithersburg, MD 20889-8422, USA*

Accepted 2022 December 15. Received 2022 December 14; in original form 2022 October 11

ABSTRACT

We report accurate Ritz wavelengths for parity-forbidden [Ni II] transitions, derived from energy levels determined using high-resolution Fourier transform spectroscopy. Transitions between the 18 lowest Ni II energy levels of even-parity produced Ritz wavelengths for 126 parity-forbidden lines. Uncertainties for the Ritz wavelengths derived in this work are up to two orders of magnitude lower than previously published values. Transition probabilities were calculated using the semi-empirical orthogonal operator method, with uncertainties ranging from approximately 1 per cent for strong M1 lines and up to 10 per cent for weak E2 lines. Accurate forbidden line wavelengths and transition probabilities, particularly for lines in the infrared, are important in the analyses of low-density astrophysical plasmas, such as supernova remnants, planetary nebulae, and active galactic nuclei.

Key words: atomic data – line: identification – methods: laboratory: atomic – techniques: spectroscopic.

1 INTRODUCTION

The majority of absorption lines observed in stellar spectra are produced by electric dipole (E1) transitions between levels of opposite parity within atoms of a star's atmosphere. In contrast, spectra of low-density astrophysical plasmas, such as those from star-forming regions, planetary nebulae, and regions around active galactic nuclei, also exhibit strong emission lines primarily generated by electron deexcitation from low-lying, long-lived metastable levels.

In general, metastable levels have the same parity as the ground state and have lower energies than any other level of opposite parity. As transitions between metastable levels and to the ground state do not involve a change in parity, deexcitation from metastable levels via E1 transitions is forbidden (as shown in Table 1) and alternative radiative mechanisms must take place. The main radiative decay mechanisms of metastable levels are through the higher order magnetic dipole (M1) and electric quadrupole (E2) transitions.

The radiative lifetimes of metastable levels are on the order of seconds, compared to nanoseconds for ordinary excited states. In laboratory and stellar plasmas, high particle densities ensure that the mean time between collisions is much shorter than the lifetimes of metastable levels, which are therefore predominantly depopulated through collisions. However, in dilute astrophysical plasmas, with low particle densities, the probability of particle collision is low and metastable levels are able to decay radiatively. As a result, parity-forbidden lines are observed in the spectra of low-density astrophysical plasmas and are important for diagnostics of these objects.

[Ni II] lines have been observed in various regions of low-density astrophysical plasmas, for example in supernova remnants (Dhawan et al. 2018; Wilk, Hillier & Dessart 2018), hot post-asymptotic giant branch (AGB) stars (Ikonnikova et al. 2020), gaseous nebulae (Lucy 1995; Bautista et al. 2006), Weigelt blobs (Zethson et al. 2012), and plasmas surrounding areas such as active galactic nuclei (Reunanen, Tacconi-Garman & Ivanov 2007). Diagnostics of these low-density plasmas, however, are usually only performed using a set of standard pairs of forbidden lines, and information contained in many other forbidden lines is rarely extracted. This is due, at least in part, to a lack of accurate atomic data for other forbidden lines.

In this paper, we present a comprehensive list of accurate Ritz wavelengths and transition probabilities for forbidden lines of Ni II. These data will allow more accurate identifications of forbidden lines in low-density astrophysical plasmas.

2 LABORATORY DATA

Previously, published Ritz wavelengths of [Ni II] were calculated from the energy levels measured by Shenstone (1970) using grating spectroscopy. As Shenstone did not include uncertainties for his levels, Sugar & Corliss (1985) estimated these uncertainties to be 0.05 cm^{-1} in their compilation of iron group element energy levels. The uncertainty of a Ritz wavenumber calculated from published energy levels is the addition in quadrature of the two level uncertainties, giving an uncertainty of 0.07 cm^{-1} for Ritz wavenumbers calculated using Shenstone's energy levels. This uncertainty is now too large for the accurate interpretation of modern, high-resolution astrophysical spectra. To address this issue, new Ritz wavelengths and wavenumbers have been calculated for transitions between the lowest known metastable levels of Ni II, up to energies of

★ E-mail: c.clear14@imperial.ac.uk

© The Author(s) 2022.
Published by Oxford University Press on behalf of Royal Astronomical Society. This is an Open Access article distributed under the terms of the Creative Commons Attribution License (https://creativecommons.org/licenses/by/4.0/), which permits unrestricted reuse, distribution, and reproduction in any medium, provided the original work is properly cited.

Downloaded from https://academic.oup.com/mnras/article/519/3/4040/6957265 by National Institutes of Standards (NIST) user on 30 June 2023

Table 1. Selection rules for allowed E1 and forbidden M1 and E2 transitions.

Type	Parity	ΔJ	ΔJ restrictions
E1	Must change	0, ±1	0↮0
M1	No change	0, ±1	0↮0
E2	No change	0, ±1 ± 2	0↮0, 1/2↮1/2, 0↮1

51045.521 cm^{-1}, using optimized energy levels determined after an extensive term analysis using Fourier transform (FT) spectroscopy by Clear et al. (2022). Energy level uncertainties for FT measured energy levels are typically at least an order of magnitude lower than those derived from grating spectra.

In the work of Clear et al. (2022), spectra of water-cooled, nickel–helium hollow cathode discharges were measured with the Imperial College London (ICL) vacuum ultraviolet (VUV) Fourier transform spectrometer (Thorne et al. 1987) in the region 15 798–75 000 cm^{-1} (133–633 nm) and with the 2-m FT spectrometer at the National Institute for Standards and Technology (NIST) in the region 9000–23 000 cm^{-1} (435–1111 nm). Additional lines in the infrared (IR) were extracted from two archive spectra, measured at the Kitt Peak National Observatory (KPNO). The cathodes used at ICL and NIST were 99.99 per cent nickel. A summary of all the spectra used in this analysis can be found in table 1 of Clear et al. (2022).

The profiles of observed spectral lines were fitted using the XGREMLIN program (Nave et al. 2015) to provide accurate wavenumbers. Lines were either fitted with Voigt profiles for symmetrical, unblended lines or with centre-of-gravity (CoG) fits for asymmetrical lines. Fitted lines were wavenumber calibrated using 26 Ar II lines between 19 429 and 23 644 cm^{-1}, recommended by Learner & Thorne (1988) and measured by Whaling et al. (1995). The wavenumber calibration was extended from the visible to the vacuum ultraviolet (VUV) and IR by nickel lines in the overlapping regions of successive spectra. The total wavenumber uncertainty of a measured line was taken to be the addition in quadrature of the uncertainty of the line fitting and the calibration correction uncertainty of its spectrum. Full details of the uncertainty analysis of observed lines are given in Clear et al. (2022).

The identified Ni II lines were then used to calculate optimized energy levels using the weighted least-squares fitting programme LOPT (Kramida 2011). Line weightings were proportional to the inverse squares of their total wavenumber uncertainties. In addition to the previously published 3d^9 and 3d^8 4s levels (Clear et al. 2022), we have optimized the metastable, doubly excited level 3d^{7}4s^2 ^{4}F$_{9/2}$ using the same method as described above. Full details of the level optimization for this level and the other doubly excited levels of Ni II will be the subject of a future publication.

The Ni II metastable energy levels used in this work were determined with uncertainties between 0.0013 and 0.0018 cm^{-1} (Clear et al. 2022) for the singly excited levels and 0.009 cm^{-1} for the newly optimized 3d^{7}4s^2 level and are shown in Table 2.

3 ANALYSIS

Ni II has a complex energy level structure, with 17 even-parity, metastable levels lying between the 3d^9 ^{2}D$_{5/2}$ ground state and the lowest energy odd-parity level, 3d^8(^{3}F)4p ^{4}D$^o_{7/2}$. The metastable levels of Ni II are shown in the partial energy level diagram Fig. 1, grouped by configuration, with individual spin–orbit (LS) terms and levels shown. The levels of the 3d^8(^{3}F)4p subconfiguration ^{4}D^o term (the lowest lying odd-parity levels of Ni II) are also shown, denoting the upper limit for the metastable energy levels.

Table 2. Ground state and metastable energy levels of Ni II from Clear et al. (2022). Energy level uncertainties are given at the one standard deviation level.

Energy level Configuration	Term	J	Energy (cm^{-1})	Unc. (cm^{-1})
3d^9	^{2}D	5/2	0.0000	0.0000
3d^9	^{2}D	3/2	1506.9621	0.0016
3d^8(^{3}F)4s	^{4}F	9/2	8393.8741	0.0014
3d^8(^{3}F)4s	^{4}F	7/2	9330.0014	0.0013
3d^8(^{3}F)4s	^{4}F	5/2	10115.5875	0.0013
3d^8(^{3}F)4s	^{4}F	3/2	10663.8120	0.0014
3d^8(^{3}F)4s	^{2}F	7/2	13550.2968	0.0013
3d^8(^{3}F)4s	^{2}F	5/2	14995.5023	0.0013
3d^8(^{3}P)4s	^{4}P	5/2	23108.1243	0.0014
3d^8(^{1}D)4s	^{2}D	3/2	23796.0234	0.0014
3d^8(^{3}P)4s	^{4}P	3/2	24788.0505	0.0014
3d^8(^{3}P)4s	^{4}P	1/2	24835.7880	0.0015
3d^8(^{1}D)4s	^{2}D	5/2	25036.2299	0.0015
3d^8(^{3}P)4s	^{2}P	3/2	29070.7363	0.0016
3d^8(^{3}P)4s	^{2}P	1/2	29593.2604	0.0016
3d^8(^{1}G)4s	^{2}G	9/2	32499.3608	0.0018
3d^8(^{1}G)4s	^{2}G	7/2	32523.3864	0.0018
3d^{7}4s^2	^{4}F	9/2	51045.521[a]	0.009

[a]This energy was derived for this work and was not published by Clear et al. (2022).

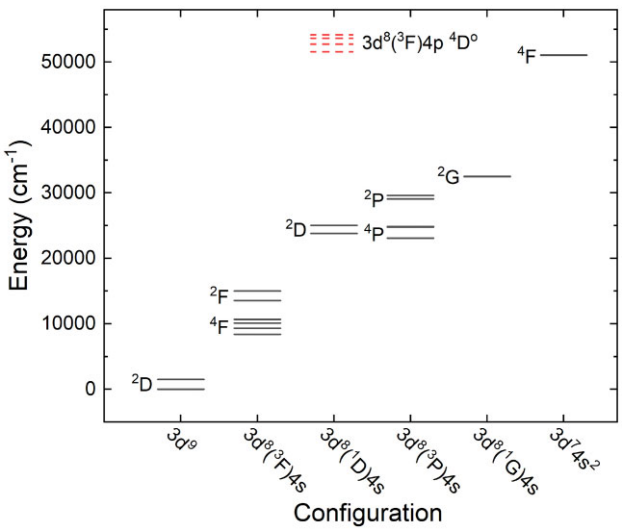

Figure 1. Partial energy level diagram showing the 3d^9 ^{2}D$_{5/2}$ ground state and 17 even-parity metastable levels of Ni II. Levels of the 3d^8(^{3}F)4p ^{4}D^o term (red dashed lines), which are the lowest energy odd-parity levels, are shown to denote the upper energy limit of the region in which E1 transitions are forbidden. Note: the 3d^8(^{3}P)4s ^{4}P$_{3/2}$ and ^{4}P$_{1/2}$ and the 3d^8(^{1}G)4s ^{2}G$_{9/2}$ and ^{2}G$_{7/2}$ energy levels lie too close to each other to be resolved in this plot. Only the ^{4}F$_{9/2}$ level of the 3d^{7}4s^2 configuration lies below the energy of the levels of the 3d^8(^{3}F)4p ^{4}D^o term.

In combination with the selection rules for M1 and E2 transitions given in Table 1, vacuum Ritz wavenumbers were calculated using LOPT and the optimized Ni II metastable energy level values. In total, wavenumbers for 126 parity-forbidden transitions were calculated and are given in Table 4. The uncertainties in the Ritz wavenumbers were calculated from the covariance matrix of LOPT and are lower and more statistically rigorous than uncertainties calculated using published energy level uncertainties. The uncertainty of the Ar II

Downloaded from https://academic.oup.com/mnras/article/519/3/4040/6957265 by National Institutes of Standards (NIST) user on 30 June 2023

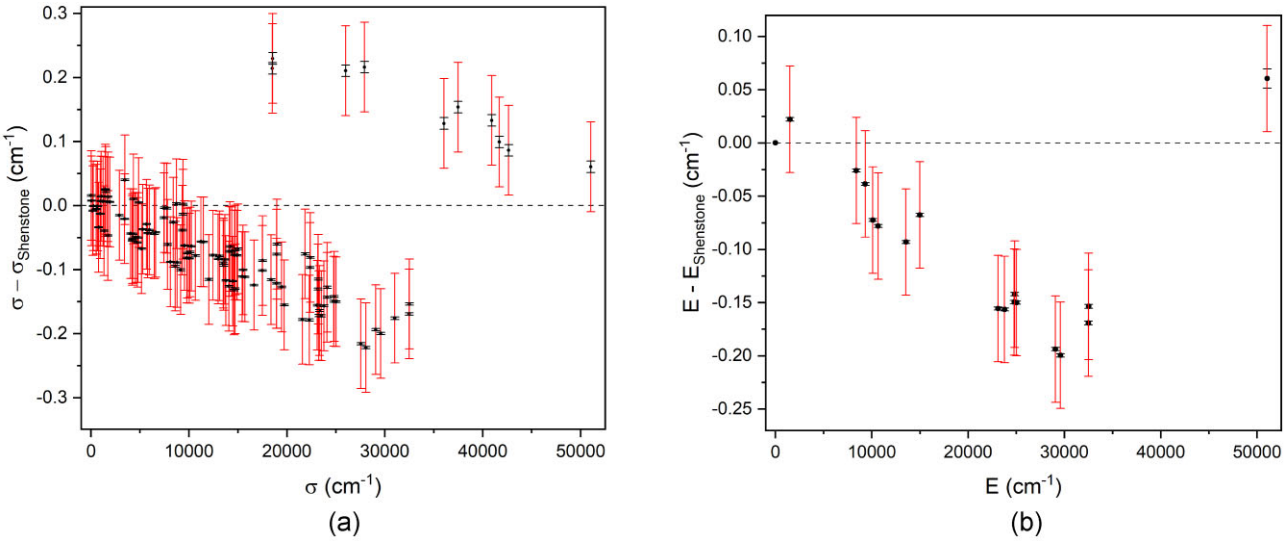

Figure 2. (a) Comparison between the [Ni II] Ritz wavenumbers in this work and those derived using the energy levels of Shenstone (1970). The uncertainties of Shenstone's Ritz wavenumbers are shown in red and our uncertainties are in black. The large reduction in uncertainty of our Ritz wavenumbers compared to previously published values can clearly be seen. (b) Comparison between the Ni II metastable energy level values of Clear et al. (2022) and the newly optimized $3d^74s^2$ level of this work and those of Shenstone (1970). The energy level value uncertainties of Shenstone (1970) and Clear et al. (2022) are shown in red and black, respectively.

standard lines used by Clear et al. (2022) for wavenumber calibration is common to all their observed lines and so becomes weighted out during the level optimization procedure. Therefore, the uncertainty of the Ar II standard lines (1×10^{-8} times the wavenumber) was added to the uncertainties of our calculated Ritz wavenumbers. A global calibration uncertainty was estimated by Clear et al. (2022) to be four parts in 10^8 and we have set this as the minimum uncertainty for all Ritz wavelengths and wavenumbers. All uncertainties are given at the one standard deviation level.

Columns 1 and 2 of Table 4 give the Ritz wavenumber of the forbidden line and its uncertainty. The vacuum Ritz wavelength, air Ritz wavelength, and wavelength uncertainty are given in columns 3–5. Air wavelengths were converted from Ritz wavenumbers using the five-parameter dispersion formula of Peck & Reeder (1972). The lower and upper energy level labels of the transition are shown in columns 6 and 7, and truncated level values are given in columns 8 and 9. Columns 10, 11, and 12 give the M1 transition probability (A^{M1}), E2 transition probability (A^{E2}), and the total transition probability (A^{tot}), respectively. The line is given as a pure M1 or E2 transition if the smaller component did not exceed 10 per cent of the total transition probability. In this case, the A^{tot} value is the dominant M1 or E2 value. Otherwise, A^{tot} is the addition of A^{M1} and A^{E2}. Column 13 shows the determined decay mechanism. The final column of Table 4 indicates astrophysical objects in which the forbidden line has been observed.

The comparison between the Ritz wavenumbers for parity-forbidden transitions in this work and those derived from the previously published energy level values of Shenstone (1970) is shown in Fig. 2(a). For the lowest wavenumbers, the difference is well within 1 standard deviation. For higher wavenumbers, however, the difference tends toward 2 standard deviations. The non-linearity of the wavenumber difference in Fig. 2(a) is reflected in the plot of the difference between the energy level values of Clear et al. (2022) and Shenstone (1970) in Fig. 2(b). The 10 wavenumbers with large positive differences with Shenstone (1970) are all transitions from the $3d^74s^2\ ^4F_{9/2}$ level, which also has a positive shift in Fig. 2(b).

Clear et al. (2022) found a shift in the wavenumber calibration of Shenstone's grating spectra in the region 50 000–60 000 cm^{-1} (167–200 nm) that contains the critical resonance lines, connecting the entire Ni II energy level system to the ground state. As a result of this shift in calibration, Shenstone's energy level values were also shifted, giving rise to the wavenumber differences seen in Fig. 2. The uncertainties of the Ritz wavenumbers in Fig. 2(a) are shown in red for Shenstone and black for our work. The clear reduction in uncertainty for our newly derived wavenumbers is up to two orders of magnitude compared to previous Ritz wavenumbers.

4 TRANSITION PROBABILITY CALCULATIONS

Previous transition probabilities of parity-forbidden Ni II lines have been calculated by several authors using a variety of methods. Nussbaumer & Storey (1982, hereafter NS) used the SUPERSTRUCTURE code of Eissner, Jones & Nussbaumer (1974), modified by Nussbaumer & Storey (1978), to calculate the term energies using a three configuration basis, with an empirical correction factor to adjust energy separations to the experimental values of Shenstone (1970).

Kurucz (2017) calculated the forbidden transitions of Ni II as part of his comprehensive calculation of atomic data for the iron group and other elements. Kurucz' atomic structure programs, based on Cowan's codes (Cowan 1981), combined least-squares fits for observed energy levels (Sugar & Corliss 1985) with computed Hartree–Fock integrals (with a large number of configurations) to calculate eigenvectors.

Quinet & Le Dourneuf (1996) used two different methods of calculation, taking into account configuration interaction and relativistic effects. The first method (referred to as SST from now on) expanded on the work of NS. Radial orbitals for SUPERSTRUCTURE were optimized using a Thomas–Fermi potential model, with wavefunctions obtained using perturbation theory, with relativistic effect corrections introduced via the Breit–Pauli approximation.

Downloaded from https://academic.oup.com/mnras/article/519/3/4040/6957265 by National Institutes of Standards (NIST) user on 30 June 2023

Table 3. Values for the electric quadrupole transition integrals $\int_0^\infty P_1\, r^2\, P_2\, \mathrm{d}r$ in Ni II calculated by means of Multi-Configuration Dirac–Hartree–Fock (MCDHF; Froese Fischer et al. 2019) including core polarization. For $3d^8$ nd, the upper row gives the 3d → 3d and the lower row the nd → nd transition integrals.

Ni II	$3d^9$	$3d^8 4s$	$3d^7 4s^2$	$3d^8 4d$	$3d^8 5s$	$3d^8 5d$	$3d^8 6s$
$3d^9$	1.42	– 2.29	–	– 1.37	0.14	– 0.60	0.07
$3d^8 4s$	– 2.29	1.18	– 1.76	8.96	–	2.79	–
$3d^7 4s^2$	–	– 1.76	1.02	–	–	–	–
$3d^8 4d$	– 1.37	8.96	–	1.14	– 37.08	– 24.07	19.98
	–	–	–	34.54	–	–	–
$3d^8 5s$	0.14	–	–	– 37.08	1.15	32.86	–
$3d^8 5d$	– 0.60	2.79	–	– 24.07	32.86	1.14	– 138.55
	–	–	–	–	–	136.58	–
$3d^8 6s$	0.07	–	–	19.98	–	– 138.55	1.14

The second method (referred to as HFR from now on) generated radial wavefunctions using the pseudo-relativistic Hartree–Fock method (Cowan 1981) with relativistic corrections introduced from a Pauli-type approximation of the Dirac–Hartree–Fock model. A semi-empirical fitting of the Slater parameters was made to match calculated energies to the experimental values of Shenstone (1970).

Most recently, Cassidy, Hibbert & Ramsbottom (2016) calculated configuration interaction wavefunctions using the CIV3 code (Hibbert 1975; Hibbert, Glass & Froese Fischer 1991) with relativistic effects modelled through the Breit–Pauli approximation. Their calculated level energies were 'fine-tuned' to the experimental values of Sugar & Corliss (1985).

In this work, the calculation of level energies and subsequent transition probabilities was achieved using the orthogonal operator method (Uylings & Raassen 2019; Uylings 2021). The calculation of transition probabilities for the iron group ions, with their open d-shells, is particularly challenging. Even when the eigenvalues exhibit general agreement with the experimental energies, the eigenvectors may still contain inaccuracies (Hibbert 2018). In most cases, magnetic effects within a particular configuration dominate in this respect, but configuration interaction cannot be neglected. Therefore, for the Ni II calculation, the even-parity model space was extended to seven configurations: $3d^9 + 3d^8\,4s + 3d^7\,4s^2 + 3d^8\,4d + 3d^8\,5s + 3d^8\,5d + 3d^8\,6s$ with a standard deviation of 7.8 cm^{-1} for the lowest three even configurations.

The diagonalization of the total energy matrix results in eigenvalues and eigenvectors. The eigenvectors $(i|SL\,J)$ and $\left(S'L'\,J'|f\right)$ of the atomic states i and f are used to transform line strengths from pure LS coupling to the actual intermediate coupling scheme:

$$S_{if} = \left| \sum_{SL\,S'L'} (i|SL\,J)\; S^{1/2}(SL\,J, S'L'\,J')\; \left(S'L'\,J'|f\right) \right|^2, \qquad (1)$$

where

$$S^{1/2}(SLJ, S'L'J') = \left\langle \Psi SL\,J \,\middle\|\, M^{(1)} \,\middle\|\, \Psi' SL\,J' \right\rangle \qquad (2)$$

$$\text{or} = \left\langle \Psi SL\,J \,\middle\|\, Q^{(2)} \,\middle\|\, \Psi'\; SL'\,J' \right\rangle \qquad (3)$$

for the magnetic dipole operator $M^{(1)}$ and the electric quadrupole operator $Q^{(2)}$, respectively. Both quantities consist of angular matrices that are calculated exactly by angular momentum algebra, but in the case of electric quadrupole radiation, a radial factor, $\int_0^\infty P_1 r^2 P_2\, \mathrm{d}r$ (where P_1 and P_2 are the single electron radial orbits involved in the transition), must also be included. The radial electric quadrupole transition integrals, specific for the ion in question, are taken from relativistic Hartree–Fock calculations and, for Ni II, are listed in Table 3. The corresponding transition probabilities (in s^{-1}) are given by

$$A_{if}^{\mathrm{M1}} = 2.697 \times 10^{-11}\, \frac{\sigma^3}{2J_\mathrm{u}+1}\, S_{if}^{\mathrm{M1}}, \qquad (4a)$$

$$A_{if}^{\mathrm{E2}} = 1.1199 \times 10^{-22}\, \frac{\sigma^5}{2J_\mathrm{u}+1}\, S_{if}^{\mathrm{E2}}, \qquad (4b)$$

where σ is the transition wavenumber (in cm^{-1}) and J_u is the J value of the upper state.

The comparison between the transition probabilities (A values) calculated in this work and previously published values is shown in Fig. 3. A values for strong lines show good agreement between the methods, especially with the values of Cassidy et al. (2016) and SST. It should be noted that all previous calculations were optimized using the energy level values of Shenstone (1970) rather than the newly published, and more accurate, level values of Clear et al. (2022) used in this work.

After calculation of the A values themselves, it is important to assess their accuracy. Some more recent references on this issue are Kramida (2014), who suggests a practical evaluation method by randomly varying atomic code input parameters, Fivet, Quinet & Bautista (2016) who compare ab initio and semi-empirical approaches and Hibbert (2018) who focuses on the mutual comparison of ab initio calculations.

A balanced discussion of accuracy should discriminate between ab initio and semi-empirical approaches, magnetic dipole and electric quadrupole transitions, strong and weak lines, and absolute versus relative accuracy. In all cases, equations (1), (4a), and (4b) can be used as a basis. Although both semi-empirical and ab initio approaches employ equations (4a) and (4b), there are differences between the methods, such as the use of experimental versus calculated σ values, the truncation of the model space (the effects of high-lying unobserved configurations not included in the model space are supposed to be small, as only the lowest energy levels are involved in M1 and E2 transitions in view of their population), and the neglect of the term dependency of quadrupole transition integrals in Table 3 (estimated to be less than 1 per cent).

A crucial difference between semi-empirical and ab initio calculations is the eigenvector composition. The advantage of the orthogonal operator method is the use of optimal eigenvector compositions, as a result of the fine-tuning of eigenvalues, including all one- and two-particle magnetic effects. This procedure requires experimental energy levels, which are more widely available for the lowest configurations.

Downloaded from https://academic.oup.com/mnras/article/519/3/4040/6957265 by National Institutes of Standards (NIST) user on 30 June 2023

Table 4. Parity-forbidden transitions of Ni II.

σ (cm^{-1})	Unc. (cm^{-1})	λ_{vac} (Å)	λ_{air} [a] (Å)	Unc. (Å)	Transition level Lower	Transition level Upper	Energy[b] Lower	Energy[b] Upper	A^{M1} (s^{-1})	A^{E2} (s^{-1})	A^{tot} [c] (s^{-1})	Type	Observed in object [d]
24.0256	0.0014	4162 230	–	240	$(^1G)4s\ ^2G_{9/2}$	$(^1G)4s\ ^2G_{7/2}$	32 499	32 523	2.09×10^{-7}	6.54×10^{-17}	2.09×10^{-7}	M1	
47.7375	0.0008	2094 791	–	36	$(^3P)4s\ ^4P_{3/2}$	$(^3P)4s\ ^4P_{1/2}$	24 788	24 836	3.63×10^{-6}	1.23×10^{-15}	3.63×10^{-6}	M1	
200.4420	0.0009	498 897.5	–	2.2	$(^3P)4s\ ^4P_{1/2}$	$(^1D)4s\ ^2D_{5/2}$	24 836	25 036	–	2.46×10^{-12}	2.46×10^{-12}	E2	
248.1795	0.0007	402 934.2	–	1.2	$(^3P)4s\ ^4P_{3/2}$	$(^1D)4s\ ^2D_{5/2}$	24 788	25 036	1.90×10^{-4}	9.00×10^{-12}	1.90×10^{-4}	M1	
522.5241	0.0009	191 378.7	–	0.3	$(^3P)4s\ ^2P_{3/2}$	$(^3P)4s\ ^2P_{1/2}$	29 071	29 593	2.50×10^{-3}	2.21×10^{-9}	2.50×10^{-3}	M1	
548.2244	0.0009	182 407.1	–	0.3	$(^3F)4s\ ^4F_{5/2}$	$(^3F)4s\ ^4F_{3/2}$	10 116	10 664	1.06×10^{-2}	1.75×10^{-10}	1.06×10^{-2}	M1	
687.8991	0.0008	145 370.16	–	0.17	$(^3P)4s\ ^4P_{5/2}$	$(^1D)4s\ ^2D_{3/2}$	23 108	23 796	5.52×10^{-3}	1.37×10^{-9}	5.52×10^{-3}	M1	
785.5862	0.0008	127 293.48	–	0.12	$(^3F)4s\ ^4F_{7/2}$	$(^3F)4s\ ^4F_{5/2}$	9330	10 116	2.77×10^{-2}	9.26×10^{-10}	2.77×10^{-2}	M1	
936.1272	0.0009	106 823.09	–	0.10	$(^3F)4s\ ^4F_{9/2}$	$(^3F)4s\ ^4F_{7/2}$	8394	9330	2.73×10^{-2}	1.47×10^{-9}	2.73×10^{-2}	M1	

[a]Calculated using the five-parameter dispersion formula of Peck & Reeder (1972). [b]Truncated energy – see Table 2 for exact energy level values. [c]A^{tot} values are the M1 or E2 values if the smaller component did not exceed 10 per cent of the total transition probability. Otherwise, A^{tot} is the addition of A^{M1} and A^{E2}. Uncertainties for transition probabilities are: 1 per cent for strong A^{M1} values; <5 per cent for weaker A^{M1} values; <5 per cent for strong A^{E2} values; and <10 per cent for weaker A^{E2} values. Strong transitions are those with A values within ∼5 per cent of the highest A value for that decay mechanism. [d]A: post-AGB star (Ikonnikova et al. 2020); C: Crab Nebula (Lucy 1995); E: η Carinae (Bautista et al. 2006; Zethson et al. 2012); G: AGN (Reunanen et al. 2007); O: Orion Nebula (Lucy 1995); P: P Cygni (Lucy 1995); S: supernovae remnants (Dhawan et al. 2018; Wilk et al. 2018). (Complete table is available as Supplementary Material.)

Obviously, the issue of lack of experimental eigenvalues does not exist in the ab initio approach, where large-scale relativistic calculations are increasingly capable of producing transition probabilities of sufficient quality for astrophysical modelling of many experimentally unknown ions (Safronova & Safronova 2011; Jönsson et al. 2017; Froese Fischer et al. 2019). To attain the desired degree of accuracy, however, complex spectra are still most successfully analysed semi-empirically either using Cowan's Slater–Condon approach (Cowan 1981) or the orthogonal operator method (Uylings & Raassen 2019; Uylings 2021) applied in this work.

The calculation of transition probabilities employing the orthogonal operator method increases in accuracy from A^{E1} to A^{E2} and finally to the most accurate, A^{M1} values. Magnetic dipole transitions do not involve a radial transition integral and absolute A^{M1} values are therefore a good criterion for the quality of eigenvectors as they are the only source of inaccuracy in the calculated transition probabilities. Without direct experimental A^{M1} values available, their uncertainty is estimated from a comparison between experimental (g_{exp}) (Sugar & Corliss 1985) and theoretical (g_{th}) g-factors calculated with the orthogonal operator eigenvectors. Calculated g-factors rely on eigenvector accuracy and are exact for pure LS coupling. For our calculation, the quantities $|g_{exp} - g_{th}|/g_{exp}$ range between 0.1 per cent and 2.0 per cent. For strong lines, the accuracy is therefore estimated to be at the 1 per cent level and better than 5 per cent for weaker transitions, as the latter are derived from less pure eigenvectors.

In the case of electric quadrupole transitions, the accuracy of the A^{E2} values is comparable with the E1 transition probabilities calculated by the same orthogonal operator technique. The latter are found to be in good agreement with accurate experimental values (Raassen & Uylings 1998; Fivet et al. 2016). This is true for the strong resonance lines (agreement better than 5 per cent) and for the weaker intercombination lines (better than 10 per cent). Compared to E1 transitions, the situation for E2 transitions is slightly more favourable, as only the lowest and most accurate eigenvectors are involved. Although the radial transition integrals are calculated relativistically and corrected for quadrupole polarization, they remain (like the E1 transition integrals) one of the principal sources of error for E2 transition probabilities.

5 CONCLUSIONS

To meet the requirements of atomic data for current and future high-resolution astronomical spectroscopy, we present a comprehensive list of accurate Ritz wavelengths and wavenumbers for parity-forbidden M1 and E2 transitions between all known metastable levels of Ni II. Uncertainties for the newly derived Ritz wavenumbers are up to two orders of magnitude lower than previously published values, ranging from 0.0007 to 0.009 cm^{-1}. Transition probabilities for all lines have been calculated using the orthogonal operator method. A-value uncertainties are estimated to be 1 per cent for strong M1 transitions and up to 5 per cent for weaker transitions. For E2 transitions, A-value uncertainties are estimated at <5 per cent for strong lines and <10 per cent for weaker transitions. We define strong transitions as those having A values within ∼5 per cent of the highest A value for that decay mechanism.

These data are of particular importance for the analysis of spectra from low-density astrophysical plasmas, especially in the IR domain wherein, due to transitions between both LS terms and fine structure levels, strong forbidden lines are observed.

Downloaded from https://academic.oup.com/mnras/article/519/3/4040/6957265 by National Institutes of Standards (NIST) user on 30 June 2023

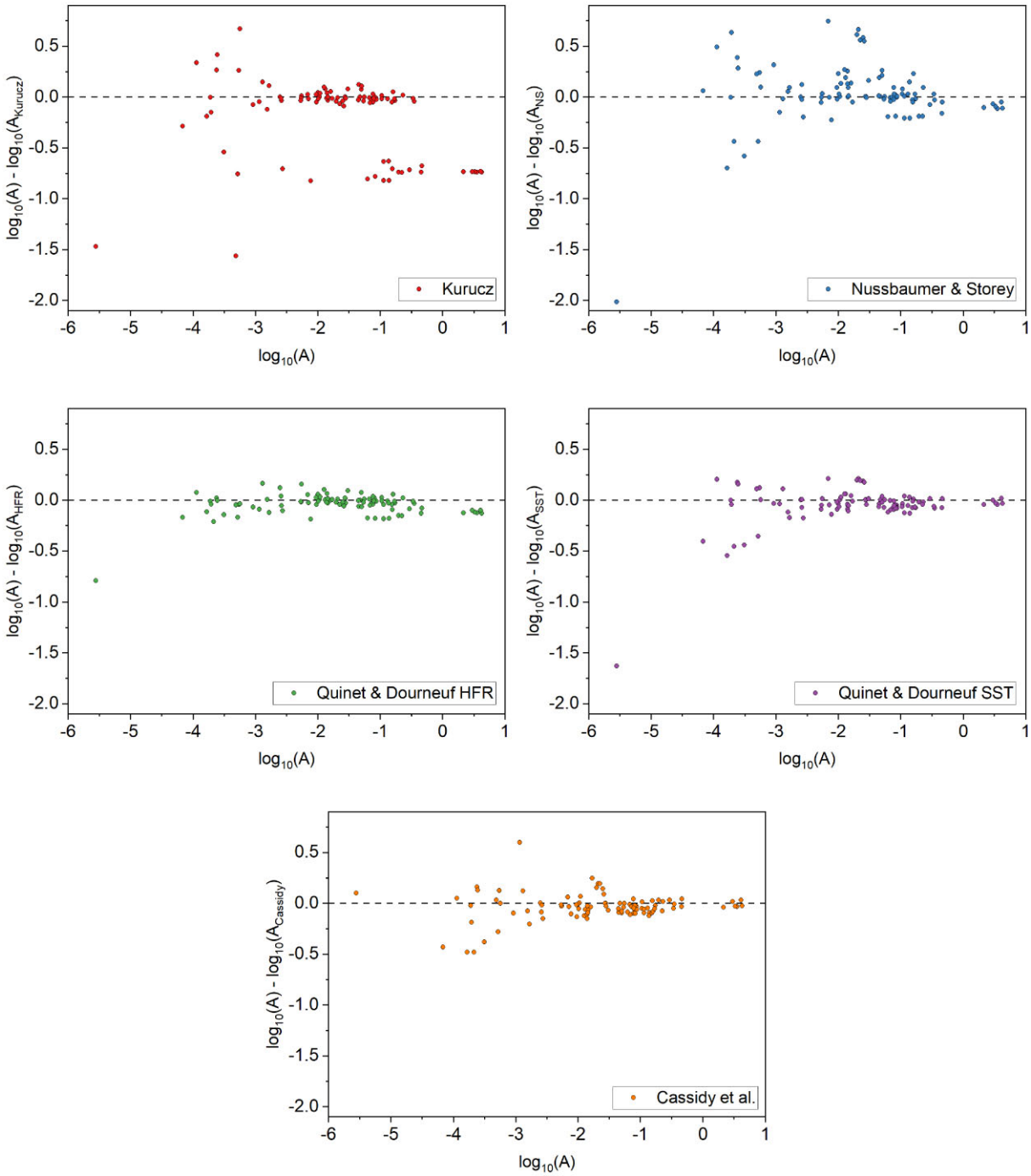

Figure 3. Comparison of transition probabilities (A) calculated in this work using the orthogonal operator method and those obtained by Kurucz (2017), Nussbaumer & Storey (1982), Quinet & Le Dourneuf (1996), and Cassidy et al. (2016).

ACKNOWLEDGEMENTS

CPC and JCP thank the STFC of the UK for their support. GN was partly supported by NASA award NNH17AE081.

DATA AVAILABILITY

The data underlying this paper will be shared on reasonable request to the corresponding author.

REFERENCES

Bautista M. A., Hartman H., Gull T. R., Smith N., Lodders K., 2006, MNRAS, 370, 1991

Cassidy C. M., Hibbert A., Ramsbottom C. A., 2016, A&A, 587, A107

Clear C. P., Pickering J. C., Nave G., Uylings P., Raassen T., 2022, ApJS, 261, 35

Cowan R. D., 1981, The Theory of Atomic Structure and Spectra. Univ. California Press, Berkeley, CA

Dhawan S., Flörs A., Leibundgut B., Maguire K., Kerzendorf W., Taubenberger S., Van Kerkwijk M. H., Spyromilio J., 2018, A&A, 619, A102

Downloaded from https://academic.oup.com/mnras/article/519/3/4040/6957265 by National Institutes of Standards (NIST) user on 30 June 2023

Eissner W., Jones M., Nussbaumer H., 1974, Comput. Phys. Commun., 8, 270
Fivet V., Quinet P., Bautista M. A., 2016, A&A, 585, A121
Froese Fischer C., Gaigalas G., Jönsson P., Bieroń J., 2019, Comput. Phys. Commun., 237, 184
Hibbert A., 1975, Comput. Phys. Commun., 9, 141
Hibbert A., 2018, Galaxies, 6, 77
Hibbert A., Glass R., Froese Fischer C., 1991, Comput. Phys. Commun., 64, 455
Ikonnikova N. P., Parthasarathy M., Dodin A. V., Hubrig S., Sarkar G., 2020, MNRAS, 491, 4829
Jönsson P. et al., 2017, Atoms, 5, 16
Kramida A. E., 2011, Comput. Phys. Commun., 182, 419
Kramida A., 2014, Atoms, 2, 86
Kurucz R., 2017, Robert L. Kurucz On-line Database of Observed and Predicted Atomic Transitions. http://kurucz.harvard.edu/atoms/2801/ (accessed 18 November 2022)
Learner R. C. M., Thorne A. P., 1988, J. Opt. Soc. Am. B, 5, 2045
Lucy L. B., 1995, A&A, 294, 555
Nave G., Griesmann U., Brault J. W., Abrams M. C., 2015, Astrophysics Source Code Library, record ascl:1511.004
Nussbaumer H., Storey P., 1978, A&A, 64, 139
Nussbaumer H., Storey P. J., 1982, A&A, 110, 295 (NS)
Peck E. R., Reeder K., 1972, J. Opt. Soc. Am., 62, 958
Quinet P., Le Dourneuf M., 1996, A&AS, 119, 99
Raassen A. J., Uylings P. H., 1998, J. Phys. B: At. Mol. Opt. Phys., 31, 3137
Reunanen J., Tacconi-Garman L. E., Ivanov V. D., 2007, MNRAS, 382, 951
Safronova U. I., Safronova M. S., 2011, Can. J. Phys., 89, 465
Shenstone A., 1970, J. Res. Natl. Bureau Standards Section A: Phys. Chem., 74A, 801
Sugar J., Corliss C., 1985, J. Phys. Chem. Ref. Data, 14, 587
Thorne A. P., Harris C. J., Wynne-Jones I., Learner R. C. M., Cox G., 1987, J. Phys. E: Sci. Instrum., 20, 54
Uylings P. H. M., 2021, Complex Atoms Described by Orthogonal Operators. Zenodo(https://doi.org/10.5281/zenodo.5710086)
Uylings P., Raassen T., 2019, Atoms, 7, 102
Whaling W., Anderson W., Carle M., Brault J., Zarem H., 1995, J. Quant. Spectrosc. Radiat. Transf., 53, 1
Wilk K. D., Hillier D. J., Dessart L., 2018, MNRAS, 474, 3187
Zethson T., Johansson S., Hartman H., Gull T. R., 2012, A&A, 540, A133

SUPPORTING INFORMATION

Supplementary data are available at *MNRAS* online.

Table 4. Parity-forbidden transitions of Ni II.

Please note: Oxford University Press is not responsible for the content or functionality of any supporting materials supplied by the authors. Any queries (other than missing material) should be directed to the corresponding author for the article.

This paper has been typeset from a TEX/LATEX file prepared by the author.

Downloaded from https://academic.oup.com/mnras/article/519/3/4040/6957265 by National Institutes of Standards (NIST) user on 30 June 2023